Microtubule dynamics regulates mitochondrial fission

Kritika Mehta[1], Manjyot Kaur Chug[1], Siddharth Jhunjhunwala[1] and Vaishnavi Ananthanarayanan[1,*]

[1] *Centre for BioSystems Science and Engineering, Indian Institute of Science, Bangalore 560012*

** To whom correspondence may be addressed. Email: vaishnavi@iisc.ac.in*

Abstract

Mitochondria are organised as tubular networks in the cell and undergo fission and fusion. Equilibrium between fission and fusion events is necessary to maintain normal mitochondrial function. While several of the molecular players involved in mediating the dynamics of mitochondria have been identified, the precise cellular cues that initiate fission or fusion remain largely unknown. In fission yeast, as in mammalian cells, mitochondrial positioning and partitioning are microtubule-mediated. In interphase, fission yeast mitochondria associate with microtubule bundles that are aligned along the long axis of the cell. Here, we perturbed microtubule dynamics via kinesin-like proteins to produce cells with long and short microtubules and observed that cells with long microtubules exhibited long, but fewer mitochondria, whereas cells with short microtubules exhibited short, but several mitochondria. We quantified that mitochondrial fission frequency correlated inversely with microtubule length. In agreement with these results, upon onset of mitosis wherein interphase microtubules assemble to form the spindle within the nucleus, we measured increased fission of mitochondria in the absence of interphase microtubules. We confirmed that partitioning of mitochondria at mitosis follows a stochastic, independent segregation mechanism and that the increase in mitochondrial fission prior to cell division therefore likely serves to increase the likelihood of equal partitioning of mitochondria between the two future daughter cells. Further, association of mitochondria with microtubules inhibited activity of the dynamin GTPase-related fission protein Dnm1, such that cells overexpressing Dnm1 but containing long microtubules were protected from increased fission. Thus, we demonstrate a general mechanism by which mitochondrial dynamics is dictated by the dynamics of the microtubule cytoskeleton.

Introduction

Mitochondria are double-membraned organelles whose functions range from ATP production to calcium signalling. Inside cells, mitochondrial form is dynamic and transitions from tubular networks to fragmented entities depending on the activity of the mitochondrial fission and fusion machinery. The major mitochondrial fission protein is dynamin-related Drp1 GTPase[1] (Dnm1 in yeast[2,3]). Multimeric Drp1 rings assemble around the mitochondrial membrane and utilize the energy from GTP hydrolysis to catalyse the constriction and fission of mitochondria[4,5]. Fusion of mitochondria requires two sets of proteins namely Opa1[6] for the inner membrane (Mgm1 in yeast[7]) and Mfn1/2[8] for the outer membrane (Fzo1 in yeast[9]).

The requirement for dynamic mitochondria has been attributed to two primary reasons, namely quality control and energy production[10]. Larger/longer mitochondria resulting from fusion are hypothesized to be capable of producing more energy whereas shorter/smaller mitochondria formed following a fission event are likely to undergo mitophagy[11]. In the case of the latter, fission could serve as an efficient mechanism to segregate and eliminate damaged mitochondria. Dysfunction of fission and fusion processes has been implicated in neurodegeneration[12,13], cancer[14] and cardiomyopathies[15], amongst a host of metabolic disorders.

In mammalian cells, mitochondria are transported along microtubule tracks by the activity of motor proteins kinesin-1 and dynein[16]. Kinesin-1 and dynein bind to the outer membrane of mitochondria via the Miro/Milton complex[17–19] and move mitochondria in the anterograde and retrograde direction respectively. In neuronal cells, increase in calcium levels results in the attachment of kinesin-1 motor to mitochondria via syntaphilin, which inhibits the ATPase activity of kinesin and hence leads to stationary mitochondria on neuronal microtubules[20]. About 70% of mitochondria in neuronal cells have been visualized in this stationary state[21].

In contrast to mammalian cells, mitochondria in fission yeast do not undergo motor-driven movement along microtubules. However, the protein Mmb1 has been identified to associate mitochondria with dynamic microtubules[22]. Upon microtubule depolymerisation using methyl benzimidazol-2-yl-carbamate (MBC) or deletion of Mmb1, mitochondria have been observed to undergo fragmentation[3,22,23]. Conversely, in cells overexpressing Mmb1, mitochondria seemingly undergo reduced fission and exhibit long mitochondria[22].

Cells employ several strategies to reduce partitioning error of organelles during mitosis, such as ordered segregation mediated by spindle poles, or increasing copy numbers of organelles prior to cell division[24]. In the latter, homogeneous distribution of the multiple organelle copies serves to increase the probability of equal partitioning stochastically. Mitochondrial inheritance has been observed to be microtubule-dependent in mammalian cells[25]. In fission yeast, mitochondrial partitioning during cell division has been proposed to be mediated by attachment of mitochondria with spindle poles[26–28], similar to the segregation of endosomes, lysosomes and Golgi bodies in mammalian cells[29,30] . However, only a portion of the observed mitochondria associated with the spindle poles[26]. Additionally, increased mitochondrial fragmentation upon the onset of mitosis has also been observed[3], perhaps indicating a stochastic mechanism for mitochondrial partitioning.

While the molecular players that effect fission and fusion have been identified in several systems, the cellular signals that regulate these events are largely elusive. Here, we demonstrate that mitochondria piggyback on dynamic microtubules to selectively undergo fission while microtubules depolymerise. Reorganisation of interphase microtubules into the nucleus when cells prepare for division also provided the cue for increased mitochondrial fission. We quantified the number of mitochondria in mother cells immediately after formation of mitotic spindle within the nucleus and the number of mitochondria in the resulting daughter cells, and confirmed that the partitioning was indeed a good fit to a binomial distribution, indicating that the mitochondria were stochastically segregated into the two daughter cells. We observed that the fission protein Dnm1 was excluded from regions of microtubules localisation and that the presence of long and stabilised microtubules was inhibitory to uncontrolled fission even when Dnm1 was overexpressed.

Results

1. Perturbation of microtubule dynamics leads to changes in mitochondrial numbers

We observed that mitochondria underwent increased fission in the absence of microtubules, but did not observe their subsequent aggregation as reported previously (Extended Data Fig. 1a-c). Instead, the fragmented mitochondria were mobile and frequently in close contact with each other (Extended Data Fig. 1b, c, Supplementary Video S1). Since the depolymerisation of microtubules had a direct effect on mitochondrial fission, we set out to study the consequence of modification of microtubule dynamics on mitochondrial dynamics. To this end, we visualised the mitochondria and microtubules of fission yeast strains carrying deletions of antagonistic kinesin-like proteins, Klp5/Klp6 and Klp4 in high-resolution deconvolved images (Fig. 1a, Supplementary Videos S2, S3 and S4).

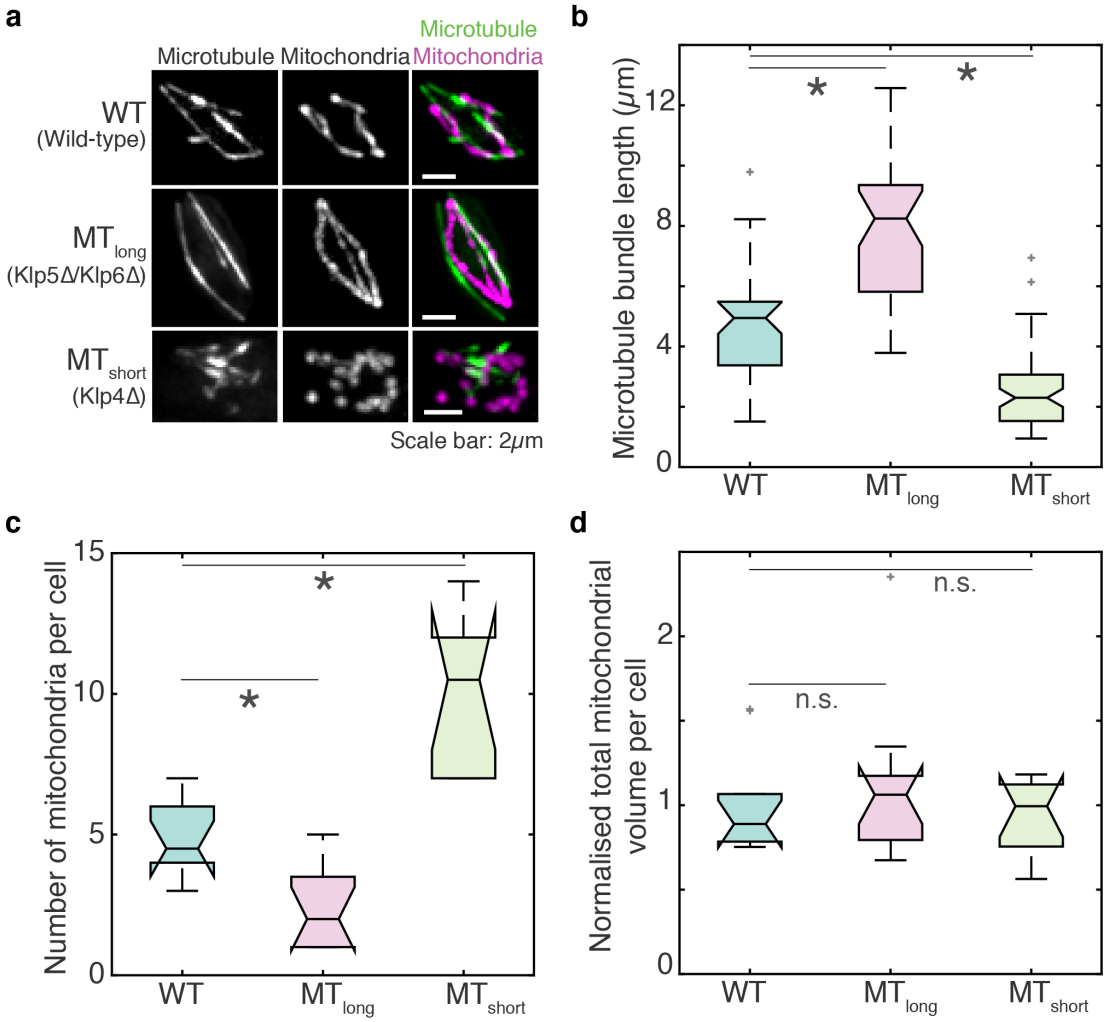

Figure 1. Mitochondrial number is inversely proportional to microtubule length. a, Maximum intensity projections of deconvolved Z-stack images of microtubules

(left), mitochondria (centre) and their composite (right) in wild-type ('WT', top, strain KI001, see Table S1), Klp5Δ/Klp6Δ ('MT_{long}', strain G3B, see Table S1) and Klp4Δ ('MT_{short}', strain G5B, see Table S1) cells. **b,** Box plot of length of anti-parallel microtubule bundles in WT, MT_{long} and MT_{short} cells (*n*=40, 37 and 63 bundles respectively). **c,** Box plot of number of mitochondria per cell in WT, MT_{long} and MT_{short} cells (*n*=10, 12 and 13 cells respectively). **d,** Box plot of the total volume of mitochondria per cell in WT, MT_{long} and MT_{short} cells normalised to mean total wild-type mitochondrial volume (*n*=10, 12 and 13 cells respectively). Light grey crosses represent outliers, asterisk represents significance ($p<0.05$) and 'n.s.' indicates no significant difference.

The heteromeric Klp5/Klp6 motor is required for maintenance of interphase microtubule length by promoting catastrophe at microtubule plus ends[31,32]. Cells lacking Klp5 and Klp6 exhibited long microtubule bundles ('MT_{long}', Fig. 1b) as reported previously due to a decreased catastrophe rate[31]. In contrast, Klp4 is required for polarised growth in fission yeast and has been suggested to promote microtubule growth[33,34]. As a result, in the absence of Klp4, microtubule bundles were only about half the length of wild-type bundles ('MT_{short}', Fig. 1b).

As in wild-type cells, mitochondria in Klp5Δ/Klp6Δ were in close contact with the microtubule, whereas we observed reduced association between the short microtubules and mitochondria in Klp4Δ cells (Fig. 1a, Supplementary Videos S3 and S4). While wild-type cells had 4.9 ± 0.4 (mean ± s.e.m.) mitochondria per cell, we observed that Klp5Δ/Klp6Δ contained only 2.3 ± 0.4 (mean ± s.e.m.). In contrast, Klp4Δ cells had 10 ± 0.9 mitochondria per cell (mean ± s.e.m., Fig. 1c). This indicated that the number of mitochondria per cell was inversely related to the length of microtubule bundle. So too, cells carrying a deletion of the EB1 homologue Mal3 exhibited small microtubule bundles[35] and also contained several mitochondria as reported previously[22] (Extended Data Fig. 1d). However, the decrease in the number of mitochondria in Klp5Δ/Klp6Δ cells and increase in Klp4Δ cells were not at the expense of mitochondrial volume, since the net mitochondrial volume in both cases was comparable to wild-type mitochondrial volume (Fig. 1d, Extended Data Fig. 1e).

2. Cells with short microtubules undergo increased fission

To understand the difference in mitochondrial numbers in wild-type, Klp5Δ/Klp6Δ and Klp4Δ cells, we acquired and analysed time-lapse videos at the single mitochondrion level in all three cases (Fig. 2a, Supplementary Videos S5, S6 and S7). Similar to our

observations from high-resolution images, we measured 3.6 ± 0.2, 2.7 ± 0.2, and 6.9 ± 0.8 mitochondria (mean ± s.e.m.) in wild-type, Klp5Δ/Klp6Δ and Klp4Δ cells respectively (Fig. 1c and 2b). Analysis of evolution of these mitochondrial numbers revealed no significant changes over time (Fig. 2b).

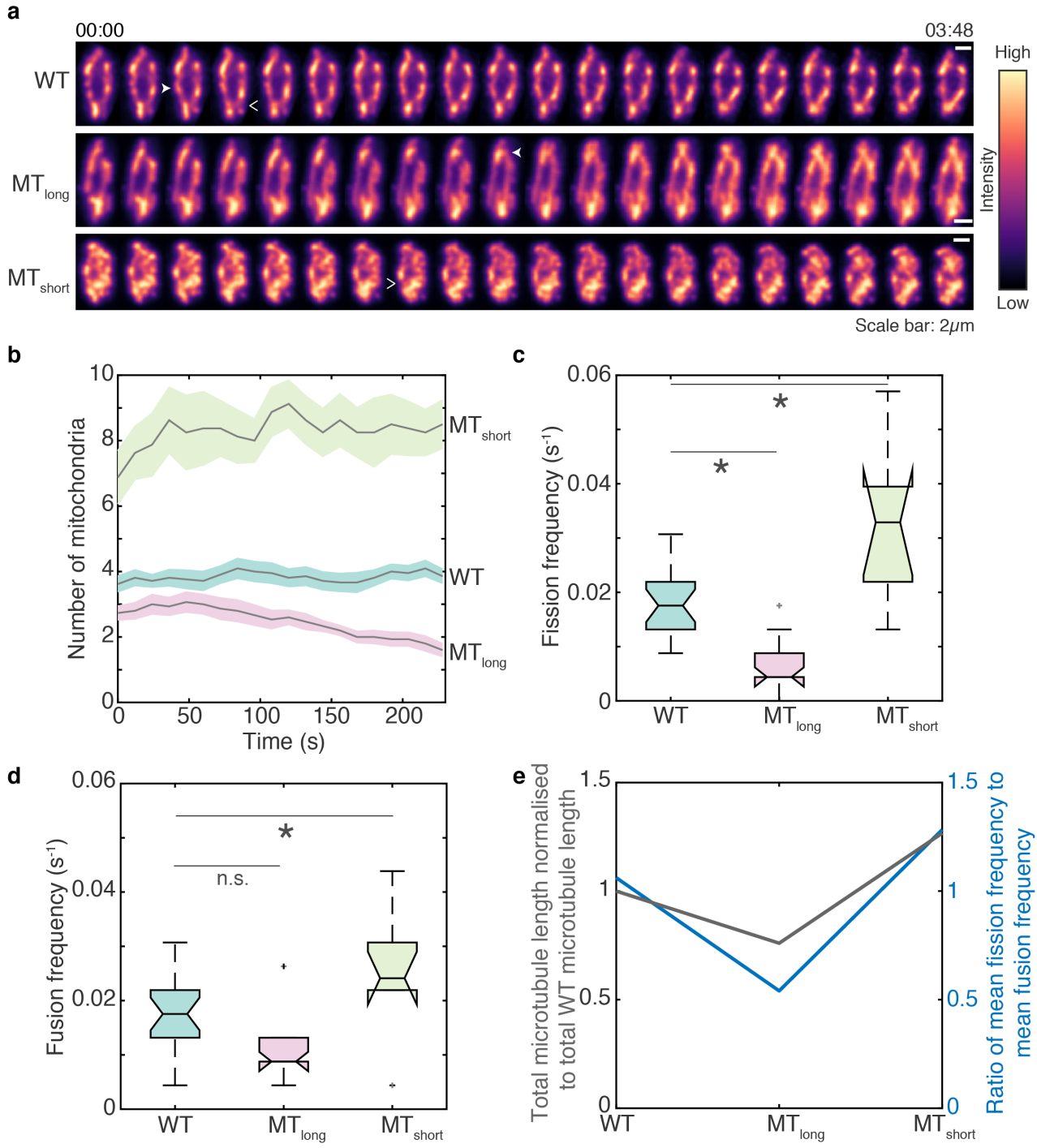

Figure 2. Microtubule catastrophe rate determines fission frequency of mitochondria. a, Montage of maximum intensity projected confocal Z-stack images of wild-type ('WT', strain KI001, see Table S1), Klp5Δ/Klp6Δ ('MT_{long}', strain G3B, see Table S1) and Klp4Δ ('MT_{short}', strain G5B, see Table S1) cells represented in the intensity map indicated to the right of the images. White solid arrowheads point to representative fusion

events and open arrowheads to fission events. Time is indicated above the images in mm:ss. **b,** Evolution of mitochondrial number over time indicated as mean (solid grey line) and standard error of the mean (shaded region) for WT, MT_{long} and MT_{short} cells (*n*=21, 15 and 8 cells respectively **c,** Box plot of the fission frequency of mitochondria per second in WT, MT_{long} and MT_{short} cells (*n*=21, 15 and 8 cells respectively). **d,** Box plot of the fusion frequency of mitochondria per second in WT, MT_{long} and MT_{short} cells (*n*=21, 15 and 8 cells respectively). Light grey crosses represent outliers, asterisk represents significance ($p<0.05$) and 'n.s.' indicates no significant difference. **e,** Plot of total microtubule length normalised to total microtubule length in wild-type cells (grey) and ratio of mean fission frequency to mean fusion frequency (blue) in WT, MT_{long} and MT_{short} cells.

Additionally, mitochondria in wild-type cells underwent ~1 fission and ~1 fusion event every minute on an average, whereas Klp5Δ/Klp6Δ cells exhibited a fission frequency that was half that of wild-type, and Klp4Δ mitochondria had a fission frequency that was almost double that of wild-type (Fig. 2c). The fusion frequency of mitochondria in Klp4Δ cells was slightly higher than in wild-type and Klp5Δ/Klp6Δ cells (Fig. 2d), likely due to the increased number of mitochondria in Klp4Δ cells that could participate in fusion. However, the resulting ratio of the mean fission frequency to the mean fusion frequency was ~1, ~0.5 and ~1.3 in wild-type, Klp5Δ/Klp6Δ and Klp4Δ cells respectively. Interestingly, these ratios accurately matched the total microtubule lengths of wild-type, Klp5Δ/Klp6Δ and Klp4Δ cells (19µm, 25µm and 15µm on an average) normalised to total WT microtubule length (1, 0.76 and 1.26 respectively, Fig. 2e). We therefore concluded that the difference in mitochondrial numbers between wild-type cells and Klp5Δ/Klp6Δ and Klp4Δ arose primarily due to the changes in fission frequencies of mitochondria. Note that the rate of mitochondrial fission (per second per mitochondrion) was comparable to the rate of mitochondrial fusion (per second per mitochondrion) in all three cases, which explains the constant number of mitochondria we measured over time (Fig. 2b).

To specifically test the role of microtubules in determining the length and dynamics of mitochondria, we depolymerised microtubules in wild-type and Klp5Δ/Klp6Δ cells and visualised the mitochondria in time-lapse movies (Extended Data Fig. 2a). In both cases, upon microtubule depolymerisation, we observed a switch in mitochondrial morphology to increased numbers and increased fission that was reminiscent of Klp4Δ cells (Extended Data Fig. 2b-h).

182 Increase in oxidative stress via reactive oxygen species (ROS) levels has also been
183 described to induce mitochondrial fission[36]. However, we measured no difference in ROS
184 levels between wild-type, Klp5Δ/Klp6Δ, and Klp4Δ cells (Extended Data Fig. 2i).
185

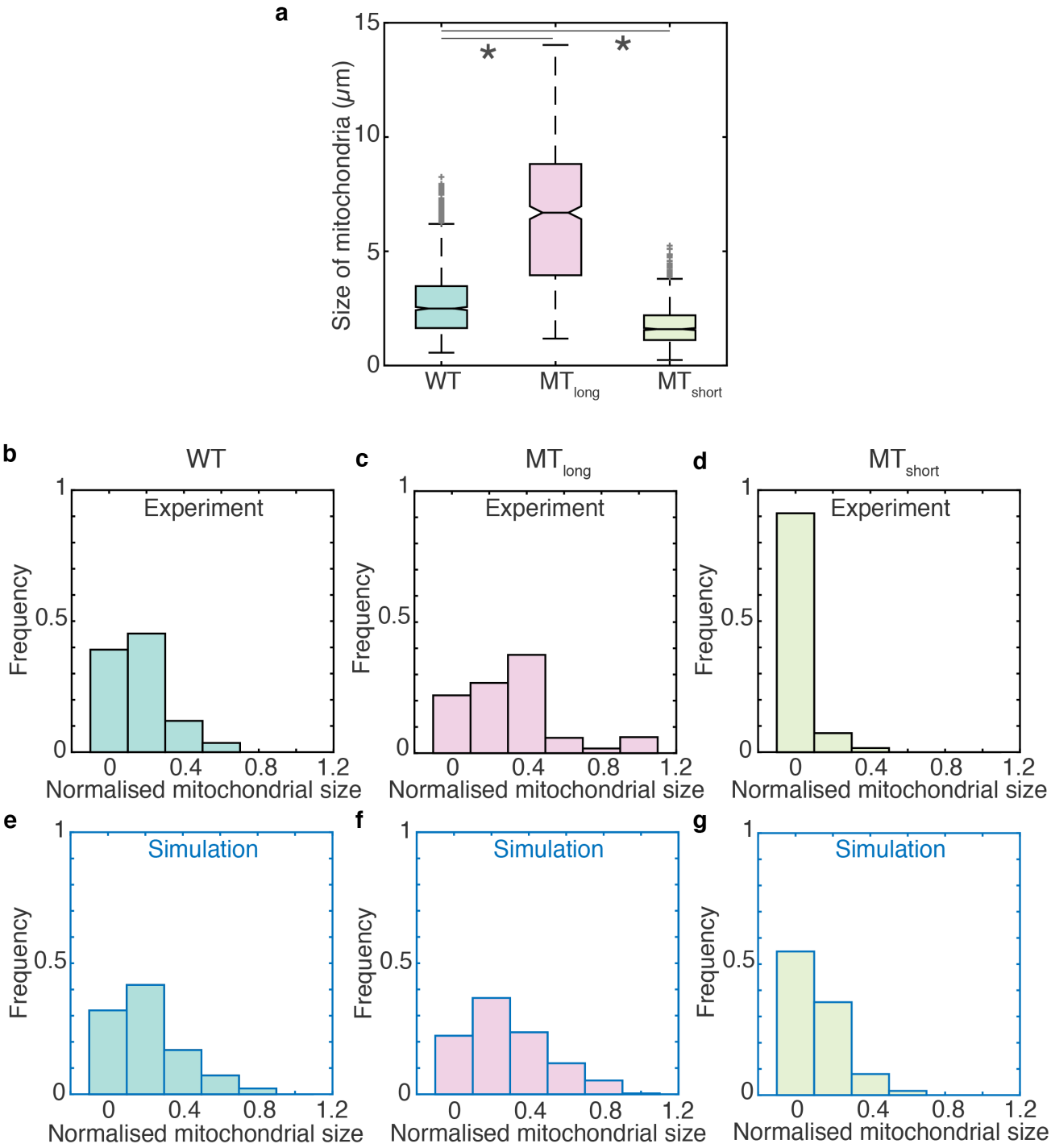

186

187 **Figure 3. Mitochondrial sizes are predicted by partitioning the same amount**
188 **of mitochondrial material among different numbers of mitochondria**. **a,** Box plot
189 of the size of mitochondria in wild-type ('WT', strain KI001, see Table S1), Klp5Δ/Klp6Δ
190 ('MT_{long}', strain G3B, see Table S1) and Klp4Δ ('MT_{short}', strain G5B, see Table S1) cells,
191 calculated as the length of the major axis of an ellipse fitted to each mitochondrion (*n*=1613,

739 and 1326 mitochondria respectively). Light grey crosses represent outliers, asterisk represents significance ($p<0.05$) and 'n.s.' indicates no significant difference. **b-d,** Histogram of mitochondrial sizes normalised to total size of mitochondria per cell obtained from experiments in WT, MT_{long} and MT_{short} cells. **e-g,** Histogram of mitochondrial sizes normalised to total size of mitochondria per cell obtained from simulations using numbers of mitochondria measured in WT, MT_{long} and MT_{short} cells.

3. Mitochondrial sizes reflect microtubule lengths

Additionally, we observed that the size of an individual mitochondrion correlated with the length of the microtubule bundle in the cell, with Klp5Δ/Klp6Δ cells containing long mitochondria and Klp4Δ cells having short mitochondria. Wild-type cells predictably exhibited mitochondrial size ranges that lay between that of Klp5Δ/Klp6Δ and Klp4Δ cells (Fig. 3a, Extended Data Fig. 3a-c). As detailed in Fig. 1d, the net mitochondrial volume was identical in wild-type, Klp5Δ/Klp6Δ and Klp4Δ cells. We tested the possibility that the mitochondrial size distributions we observed in wild-type, Klp5Δ/Klp6Δ and Klp4Δ cells (Fig. 3b-d) could simply be a consequence of partitioning the same amount of mitochondria into ~4, ~2 and ~7 mitochondria respectively. Fig. 3e-g depicts the results of simulating the possible size distributions that mitochondria could exhibit relative to the total mitochondrial size (see Methods).

We observed similar mitochondrial size distributions in both our experiments and simulations reconfirming our earlier observation that the total mitochondrial content remains unchanged between wild-type, Klp5Δ/Klp6Δ and Klp4Δ cells.

4. Mitochondria undergo stochastic partitioning during mitosis

Fission yeast undergoes closed mitosis, wherein the nuclear envelope does not undergo breakdown during cell division[37]. Upon onset of mitosis in fission yeast, the interphase microtubules that were previously in the cytoplasm are reorganised to form the spindle inside the closed nucleus. This natural situation mimics the depolymerisation of microtubules via the chemical inhibitor MBC. Therefore, we set out to study the changes in the mitochondrial network upon cell entry into mitosis. We first obtained high-resolution deconvolved images of the microtubule and mitochondria in fission yeast cells undergoing cell division (Fig. 4a, Extended Data Fig. 4a, Supplementary Video S8). We observed that dividing wild-type cells had ~4x the number of mitochondria in interphase cells (Fig. 4b). Moreover, similar to what was seen in cells lacking microtubules or Klp4 (Fig. 1a),

mitochondria in dividing cells were shorter and more rounded (Fig. 4a, Extended Data Fig. 4a). There was no relationship between length of the mitotic spindle and the number of mitochondria (Fig. 4b, Extended Data Fig. 4a), indicating that the increased fission likely occurred fairly early upon entry into mitosis. Analysis of time-lapse videos of wild-type cells before and 10min after entry into mitosis revealed a doubling of mitochondrial numbers in this time (Fig. 4c, d, Supplementary Video S9). Note that this is likely an underestimate since we were unable to reliably resolve some of the mitochondria in these lower-resolution images. The fragmented mitochondria appeared more mobile and were able to traverse distances of ~1µm in the cell presumably by Brownian motion (Fig. 4c). In this same period of time, non-dividing interphase cells did not show any change in mitochondrial numbers (Extended Data Fig. 4b, c).

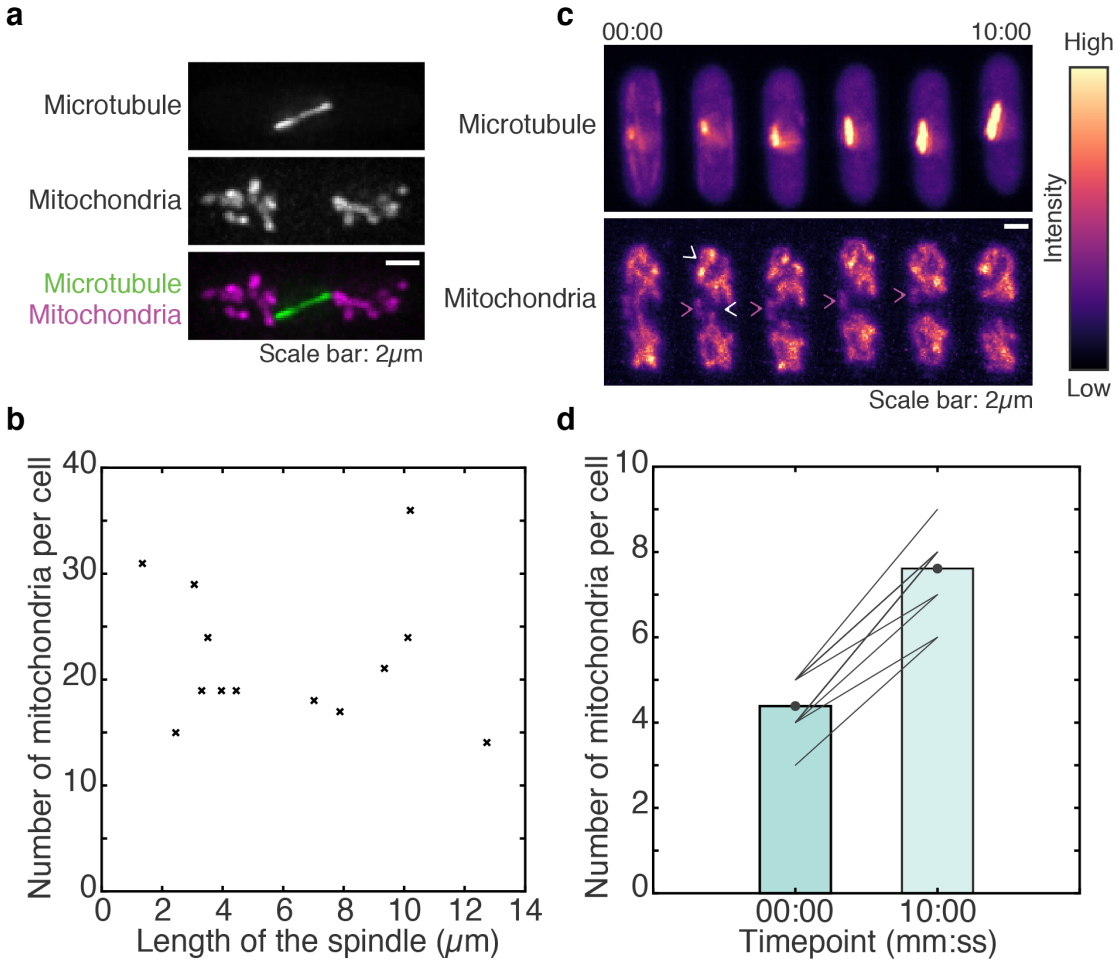

Figure 4. Mitotic cells contain several short mitochondria. a, Maximum intensity projections of deconvolved Z-stack images of the microtubules (top), mitochondria (centre) and their composite (bottom) of a wild-type cell (strain KI001, see Table S1) undergoing division. **b,** Scatter plot of the length of the mitotic spindle vs. the number of mitochondria per cell in dividing cells (*n*=13 cells). **c,** Montage of maximum intensity projected confocal Z-stack images of the microtubules (top) and mitochondria (bottom) in a wild-type cell

(strain KI001, see Table S1) undergoing cell division represented in the intensity map indicated to the right of the images. White open arrowheads point to representative fission events. Magenta arrowheads point to a representative mobile, fragmented mitochondrion. Time is indicated above the images in mm:ss. **d,** Bar plot of the mean number of mitochondria per cell before ('00:00') and 10mins after ('10:00') the onset of mitosis. Solid grey lines represent data from individual cells (*n*=16 cells).

Increase in mitochondrial numbers prior to cell division could aid in increasing the likelihood of equal partitioning of mitochondria between daughter cells, given a stochastic mechanism. To test if mitochondria in our system underwent stochastic, independent segregation,[24] with each mitochondrion in the mother cell having a 50% chance of segregating to either of the future daughter cells during mitosis, we tested the fit of our data to a binomial distribution[38] using a Chi-square test as previously described[39]. Our data (Table S2) did not differ significantly from a binomial distribution with a Chi-square statistic of 7.1846 with 3 degrees of freedom and p=0.0662, indicating that mitochondria in fission yeast were indeed segregating stochastically during cell division. The increase in mitochondrial numbers upon onset of mitosis also served to reduce the partitioning error of mitochondria between the daughter cells as predicted by stochastic segregation (Extended Data Fig. 4d).

5. Dnm1 rings do not localize to the microtubules

Taken together, our results suggest that association of mitochondria with microtubules inhibits mitochondrial fission. The mitochondrial fission protein in yeast is a dynamin-related GTPase, Dnm1[3]. Dnm1 brings about the fission of mitochondria by self-assembling into a ring around the diameter of the mitochondria and employing its GTPase activity to effect the scission[4]. In the absence of Dnm1, mitochondria are organised as extended, fused 'nets'[3,40]. We hypothesised that the binding of mitochondria to microtubules physically hinders the formation of a complete ring of Dnm1 around the mitochondrion. To test this hypothesis, we introduced GFP-tagged Dnm1 under the control of the thiamine-repressible nmt1 promoter[41] into wild-type cells expressing fluorescent microtubules (see Table S1). C- or N-terminal tagging of Dnm1 renders it inactive[3] and therefore the scission activity of Dnm1 could not be directly observed (Extended Data Fig. 5a). However, we visualised the localisation of Dnm1 'spots', representing Dnm1 assemblies. We counted a slight decrease in Dnm1 spots in Klp5Δ/Klp6Δ, and ~2x increase in Klp4Δ cells as compared to wild-type cells (Extended Data Fig. 5b), corroborating our previous observations indicating decreased

fission in the former and increased fission in the latter (Fig. 2c). Although almost 100% of the Dnm1 spots colocalised with mitochondria (Extended Data Fig. 5a), 85% of the spots did not localise on the microtubule (Fig. 5a, Supplementary Video S10), indicating that the presence of microtubule had an inhibitory effect on the assembly of the Dnm1 ring.

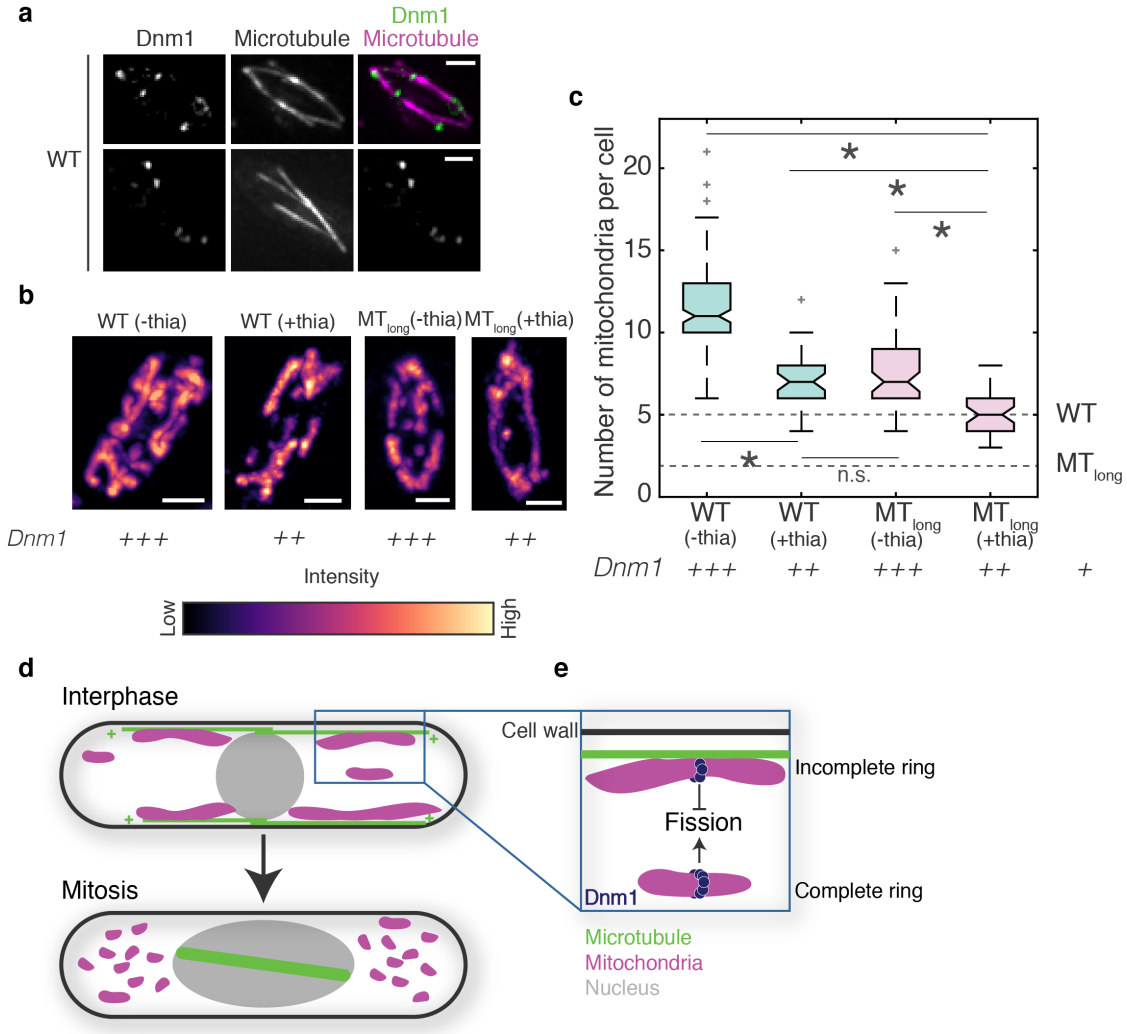

Figure 5. Association with microtubules prevents uncontrolled fission of mitochondria. a, Maximum intensity projections of deconvolved Z-stack images of Dnm1 (left), microtubules (centre) and their composite (right) in wild-type cells expressing fluorescent Dnm1 and tubulin (strain MTY271 transformed with pREP41-Dnm1-Cterm-GFP, see Table S1). A majority of Dnm1 spots did not localise on the microtubule (*n*=14 cells). **b,** Maximum intensity projections of deconvolved Z-stack images of mitochondria in cells transformed with functional untagged Dnm1 (plasmid pREP41-Dnm1, see Table S1) in wild-type ('WT', strain FY7143, see Table S1) and Klp5Δ/Klp6Δ cells ('MT_{long}', strain FY20823, see Table S1) represented in the intensity map indicated to the bottom of the images. High overpexpression of Dnm1 is indicated with '*+++*' ('WT(-thia)', and 'MT_{long}(-thia)') and low overexpression with '*++*' ('WT(+thia)', and 'MT_{long}(+thia)'). **c,** Box plot of mitochondrial numbers in WT and MT_{long} cells with high overexpression ('*+++*') or low expression of Dnm1 ('*++*') (*n*= 149, 37, 63, 41 cells respectively). The mitochondrial numbers in WT and MT_{long} cells expressing normal amount of Dnm1 ('*+*') are depicted by the dashed lines. Light

297 grey crosses represent outliers, asterisk represents significance ($p<0.05$). **d,** Model of
298 mitochondrial dynamics mediated by microtubule dynamics. Microtubules polymerise and
299 depolymerise at their plus ends ('+'). Absence of microtubule bundles in the cytoplasm
300 during cell division enables the fragmentation of mitochondria. **e,** When mitochondria are
301 bound to microtubules, Dnm1 ring assembly might be inhibited. Upon microtubule
302 depolymerisation, this inhibition is alleviated and Dnm1 can effectively mediate scission of
303 mitochondria.
304
305 To test the influence of microtubule dynamics and in essence, microtubule lengths
306 on the fission-fusion status of mitochondria, we transformed wild-type and Klp5Δ/Klp6Δ
307 cells with a plasmid expressing untagged Dnm1 under the control of the nmt1 promoter
308 (see Table S1) and visualized the mitochondria (Fig. 5b). In these cells, Dnm1 shows high
309 overexpression in the absence of thiamine and low overexpression in the presence of
310 0.05μM thiamine in the culture medium. We counted the number of mitochondria present in
311 these cells and estimated that wild-type cells highly overexpressing Dnm1 exhibited 11.6 ±
312 0.2 mitochondria (mean ± s.e.m), which is twice that of wild-type cells expressing normal
313 levels of Dnm1 (Fig. 5c). The increase in mitochondrial numbers in these cells is due to the
314 increase in Dnm1 numbers, that likely accelerates the kinetics of the Dnm1 ring formation
315 and hence, mitochondrial fission. In wild-type cells that were grown in the presence of
316 thiamine, the mitochondrial number was 7 ± 0.3 (mean ± s.e.m.), presumably because of
317 low overexpression of Dnm1. Interestingly, in Klp5Δ/Klp6Δ cells with high and low
318 overexpression of Dnm1, we counted only 7.5 ± 0.3 mitochondria and 5.2 ± 0.2
319 mitochondria (mean ± s.e.m.) respectively. In Klp5Δ/Klp6Δ, the presence of longer
320 microtubules than wild-type cells possibly prevented increased fission of mitochondria even
321 when cells overexpressed Dnm1. In fact, in Klp5Δ/Klp6Δ cells where there was low
322 overexpression of Dnm1, the mitochondrial number was comparable to that in wild-type
323 cells expressing normal levels of Dnm1 (Fig. 5c).
324 Extended Data Fig. 5c contains a summary of the mitochondrial parameters
325 measured in this study.
326
327 **Discussion**
328 We discovered that microtubule dynamics is a strong determinant for mitochondrial
329 dynamics and thereby, morphology. Mitochondrial fission frequency was proportional to
330 microtubule catastrophe rate. While previous studies discounted the role of motors in the
331 determination of mitochondrial positioning in fission yeast[23,26,42,43], we have identified

332 kinesin-like proteins that regulate mitochondrial morphology through their control over
333 microtubule length. The distribution of mitochondrial sizes that we observed in wild-type
334 cells and cells with long and short microtubules could be explained by the allocation of the
335 same amount of mitochondria between different numbers of mitochondria. We observed the
336 maximum number of mitochondria, and thereby the smallest mitochondrial sizes, in cells
337 with short microtubules.

338 We propose that equilibrium between fission and fusion of mitochondria in
339 interphase cells can be maintained solely by the inherent dynamic instability of
340 microtubules. Perturbation of microtubule dynamics shifts the balance between fission and
341 fusion frequencies to a different set point, leading to modification of mitochondrial numbers
342 and morphology. In mammalian cells, mitochondria employ microtubule-associated
343 machinery to traverse the cell. In HeLa cells, Drp1 recruitment to the mitochondria was
344 observed to be dependent on dynein[44]. Mobile mitochondria on microtubules have also
345 been seen to participate in kiss-and-run fusions that are transient[45]. Additionally, the role of
346 microtubule-stabilizing and destabilizing drugs has been tested on the biogenesis of
347 mitochondria[46]. In taxol-treated cells, mitochondria appeared more elongated whereas in
348 nocodazole-treated cells, mitochondria seemed fragmented[46]. However, a direct role for
349 microtubule localization on mitochondrial fission has not been explored.

350 We observed that fission yeast cells fragment mitochondria by emptying the
351 cytoplasm of its microtubules upon onset of mitosis, thereby ensuring stochastic
352 partitioning[38] of the several small mitochondria between future daughter cells (Fig. 5d). The
353 increase in mitochondrial numbers prior to cell division likely serves to create a well-mixed,
354 homogeneous cytoplasm that is primed for stochastic segregation of mitochondria.
355 Mitochondrial fragmentation also reduces the partitioning error between the daughter
356 cells[39], since mitochondrial numbers of 5 or less, which is typical of wild-type interphase
357 cells, exhibit errors between ~45 and 100% (Extended Data Fig. 4d). While fission yeast
358 cells employ this strategy, mammalian cells might additionally employ motor proteins to
359 actively segregate mitochondria during cell division.

360 We observed that Dnm1 spots were excluded from microtubules. We propose the
361 failure of Dnm1 ring assembly in the presence of microtubules as the nexus between
362 microtubule dynamics and mitochondrial dynamics (Fig. 5e). Previously, cryo-electon
363 tomographic analysis in fission yeast indicated a preferred separation distance of ~20nm for

364 mitochondria associated with microtubules[47]. So too, cryo-elctron microscopy in budding
365 yeast revealed that Dnm1 assembled into rings with an outer diameter of 129nm and lumen
366 diameter of 89nm, resulting in ~20nm-high structures around mitochondria[48]. Therefore,
367 mitochondria associated with microtubules might have insufficient space to accommodate
368 the Dnm1 ring around their diameter, thereby inhibiting fission due to simple physical
369 constraints.

370 Alternatively, increased fission upon microtubule depolymerization might be brought
371 about by phosphorylation of the mitochondrial fission protein Dnm1. Mammalian Drp1
372 undergoes phosphorylation at S616 mediated by Cdk1/cyclin B during cell division and
373 increases mitochondrial fission[49]. Fission yeast Dnm1 however lacks this phosphorylation
374 site. Drp1 also contains another phosphorylation site at S637, which is conserved in Dnm1.
375 However, PKA-mediated phosphorylation at S637 has been shown to inhibit fission by
376 Drp1[50], whereas Ca+/calmodulin-dependent protein kinase α-dependent phosphorylation of
377 Drp1 S637 in rat hippocampal neurons was shown to increase fission[51]. To date, yeast
378 Dnm1 has not been demonstrated to undergo phosphorylation at this site. Future studies
379 will help delineate whether the increased fission upon microtubule depolymerization is due
380 to a simple physical impediment to the assembly of Dnm1 ring or a more complex
381 biochemical signal tethered to microtubules that changes the phosphorylation status of
382 Dnm1 to activate it.

383 We also observed that the presence of long microtubules was inhibitory for fission of
384 mitochondria even in the overexpression of the fission protein Dnm1. Wild-type cells
385 contained the same total amount of mitochondria as cells with long microtubules, but
386 exhibited increased mitochondrial fission in the presence of increased Dnm1 levels. In
387 disease states such as cancer[52] and neurodegeneration[53], mitochondrial fragmentation has
388 been linked with overexpression of Drp1 in mammalian cells. In this work, we have
389 identified that cells that present increased microtubule stabilization are able to overcome
390 the effect of Dnm1 overexpression.

391 Destabilisation of microtubules is a hallmark of several neurodegenerative disorders
392 including Alzheimer's, Parkinson's and Huntington's disease[54]. So too, colorectal cancer
393 has been characterised by the absence of the tumour suppressor gene APC, which also
394 modulates microtubule dynamics[55]. Remarkably, all these disease states have also been
395 correlated with dysfunction of mitochondrial dynamics[11,56]. In future, it would be interesting

396 to investigate the effect of restoration of microtubule dynamics on the mitochondrial fission
397 and fusion in these scenarios, and consequently on the disease states.

398 **Methods**

399 **Strains and media.** The fission yeast strains used in this study are listed in Table S1. All
400 the strains were grown in YE (yeast extract) media or Edinburg Minimal media (EMM)[57] with
401 appropriate supplements at a temperature of 30˚C. Cells that were transformed with
402 pREP41-Dnm1-Cterm-GFP or pREP41-Dnm1 (see below) were cultured in EMM with
403 appropriate supplements and 0.05μM thiamine for partial induction of the nmt1 promoter.

404 **Plasmid transformation.** Transformation of strains MTY271, FY7143, FY20823 and
405 Mcl438 with plasmid pREP41-Dnm1-Cterm-GFP and pREP41-Dnm1 (see Table S1) was
406 carried out using the improved protocol for rapid transformation of fission yeast[58]. In brief,
407 cells were grown overnight to log phase in low glucose EMM, pelleted and washed with
408 distilled water. The cells were then washed in a solution of lithium acetate/EDTA (100mM
409 LiAc, 1mM EDTA, pH 4.9) and re-suspended in the same solution. 1μg of plasmid DNA was
410 added to the suspension, followed by addition of lithium acetate/PEG (40% w/v PEG,
411 100mM LiAc, 1mM EDTA, pH 4.9) and then incubated at 30°C for 30 min. This was
412 followed by a heat shock of 15min at 42°C. Thereafter, cells were pelleted down, re-
413 suspended in TE solution (10mM Tris-HCl, 1mM EDTA, pH 7.5) and plated onto selective
414 EMM plates.

415 **Preparation of yeast for imaging.** For imaging mitochondria, fission yeast cells were
416 grown overnight in a shaking incubator at 30°C, washed once with distilled water, and
417 stained with 200nM Mitotracker Orange CMTMRos (ThermoFisher Scientific, Cat. #M7510)
418 dissolved in EMM for 20min. Following this, cells were washed thrice with EMM and then
419 allowed to adhere on lectin-coated (Sigma-Aldrich, St. Louis, MO, Cat. #L2380) 35mm
420 confocal dishes (SPL, Cat. #100350) for 20min. Unattached cells were then removed by
421 washing with EMM. In experiments where mitochondria were not imaged, staining with
422 Mitotracker was omitted.

423 **Microtubule depolymerisation.** For depolymerisation of microtubules, cells were
424 treated with methyl benzimidazol-2-yl-carbamate (MBC, Carbendazim 97%, Sigma Aldrich).
425 A stock solution with a concentration of 25mg/ml was prepared in DMSO and later diluted to
426 a working concentration of 25μg/ml in EMM.

427 **Microscopy.** Confocal microscopy was carried out using the InCell Analyzer-6000 (GE
428 Healthcare, Buckinghamshire, UK) with 60x/0.7 N.A. objective fitted with an sCMOS 5.5MP

429 camera having an x-y pixel separation of 108nm. For GFP and Mitotracker Orange imaging,
430 488 and 561nm laser lines and bandpass emission filters 525/20 and 605/52nm
431 respectively were employed. Time-lapses for visualisation of mitochondrial dynamics were
432 captured by obtaining 5 Z-stacks with a 0.5μm-step size every 12s. Deconvolution was
433 performed in images obtained using a Deltavision RT microscope (Applied Precision) with a
434 100×, oil-immersion 1.4 N.A. objective (Olympus, Japan). Excitation of fluorophores was
435 achieved using InsightSSI (Applied Precision) and corresponding filter selection for
436 excitation and emission of GFP and Mitotracker Orange. Z-stacks with 0.3μm-step sizes
437 encompassing the entire cell were captured using a CoolSnapHQ camera (Photometrics),
438 with 2X2 binning. The system was controlled using softWoRx 3.5.1 software (Applied
439 Precision) and the deconvolved images obtained using the built-in setting for each channel.
440 **3D visualisation of deconvolved images**. 3D views of the microtubules and
441 mitochondria in Supplementary Movies S2, S3, S4, S8, S9 and S10 were obtained from
442 deconvolved images captured in the Deltavision microscope using Fiji's '3D project'
443 function, with the brightest point projection method and 360˚ total rotation with 10˚ rotation
444 angle increment.
445 **Estimation of volume of mitochondria.** Mitochondrial volume was estimated in Fiji by
446 integrating the areas of mitochondria in thresholded 3D stacks of cells in fluorescent
447 deconvolved images obtained using the Deltavision RT microscope. The total volume was
448 then normalised to the mean total mitochondrial volume of wild-type cells. Individual
449 mitochondrial volumes were estimated in the same fashion.
450 **Analysis of mitochondrial dynamics.** Individual mitochondria were identified in each
451 frame of the time-lapse obtained in confocal mode of the GE InCell Analyzer after projecting
452 the maximum intensity of the 3D stack encompassing the cell, followed by mean filtering
453 and visualisation in Fiji's 'mpl-magma' lookup table. Following identification of mitochondria,
454 the 'Measure' function of Fiji was employed to obtain the circularity, aspect ratio and
455 parameters of fitted ellipse. The length of the major axis of the ellipse fitted to a
456 mitochondrion was defined as the size of that mitochondrion. The size, circularity and
457 aspect ratio were estimated for mitochondria at each frame and each time point. Fission
458 and fusion frequencies of mitochondria were estimated by counting the number of
459 mitochondria identified during each frame of the time-lapse. The difference in number of
460 mitochondria from one frame to the next was counted, with an increase being counted as

461 fission event and decrease as fusion event. The total number of fission events and fusion
462 events per cell were estimated and divided by the total duration of the time-lapse to obtain
463 the fission and fusion frequencies.

464 **Simulation of mitochondrial size distribution.** Mitochondrial size distributions in
465 wild-type, Klp5Δ/Klp6Δ and Klp4Δ cells were simulated by taking experimentally measured
466 mitochondrial numbers in the three cases and assuming that the total mitochondrial amount
467 was the same. Briefly, to make the system amenable to simulation using an integer-
468 partitioning problem, the total mitochondrial amount was taken to be a constant of 10. The
469 minimum size of mitochondria that could be present was assumed to be 1. The total
470 mitochondria was then partitioned between the available mitochondrial numbers in wild-
471 type, Klp5Δ/Klp6Δ and Klp4Δ cells of ~4, ~2 and ~7 in units of 1. The distributions were
472 then normalised to total mitochondrial amount to get mitochondrial sizes as fractions of the
473 total mitochondrial content. The minimum mitochondrial size thus obtained in this case, 0.1,
474 is similar to experimentally obtained normalised minimum mitochondrial sizes.

475 **Test for fit of mitochondrial partitioning during mitosis to binomial**
476 **distribution.** To test the fit of mitochondrial segregation during mitosis to a binomial
477 distribution, the data were z-transformed as previously described[39]. Briefly, given n
478 mitochondria in the mother cell just prior to cell division, x and $n - x$ mitochondria in the
479 resulting daughter cells, z was given by $2x - n/\sqrt{n}$ to approximate the binomial distribution
480 to a normal distribution of 0,1. The z values obtained for each x and n were binned into k
481 bins of equal sizes and subjected to Chi-square test with $k - 1$ degrees of freedom. The z
482 values are expected to be equally distributed among the k bins, with expected number of
483 $1/k$ per bin.

484 **Data analysis and plotting.** Data analysis was performed in Matlab (Mathworks, Natick,
485 MA). Box plots with the central line indicating the median and notches that represent the
486 95% confidence interval of the median were obtained by performing one-way ANOVA
487 ('anova1' in Matlab). Following this, significance ($p<0.05$) of the means was tested using
488 the Tukey-Kramer post-hoc test. All the plots were generated using Matlab.

489

490 **References**

491 1. Smirnova, E., Griparic, L., Shurland, D. L. & van der Bliek, A. M. Dynamin-related
492 protein Drp1 is required for mitochondrial division in mammalian cells. *Mol. Biol. Cell*
493 **12,** 2245–56 (2001).

494 2. Bleazard, W. *et al.* The dynamin-related GTPase Dnm1 regulates mitochondrial
495 fission in yeast. *Nat. Cell Biol.* **1,** 298–304 (1999).
496 3. Jourdain, I., Gachet, Y. & Hyams, J. S. The dynamin related protein Dnm1 fragments
497 mitochondria in a microtubule-dependent manner during the fission yeast cell cycle.
498 *Cell Motil. Cytoskeleton* **66,** 509–523 (2009).
499 4. Ingerman, E. *et al.* Dnm1 forms spirals that are structurally tailored to fit mitochondria.
500 *J. Cell Biol.* **170,** 1021–7 (2005).
501 5. Basu, K. *et al.* Molecular mechanism of DRP1 assembly studied in vitro by cryo-
502 electron microscopy. *PLoS One* **12,** e0179397 (2017).
503 6. Delettre, C. *et al.* Nuclear gene OPA1, encoding a mitochondrial dynamin-related
504 protein, is mutated in dominant optic atrophy. *Nat. Genet.* **26,** 207–210 (2000).
505 7. Sesaki, H., Southard, S. M., Yaffe, M. P. & Jensen, R. E. Mgm1p, a dynamin-related
506 GTPase, is essential for fusion of the mitochondrial outer membrane. *Mol. Biol. Cell*
507 **14,** 2342–56 (2003).
508 8. Eura, Y., Ishihara, N., Yokota, S. & Mihara, K. Two Mitofusin Proteins, Mammalian
509 Homologues of FZO, with Distinct Functions Are Both Required for Mitochondrial
510 Fusion. *J. Biochem.* **134,** 333–344 (2003).
511 9. Hermann, G. J. *et al.* Mitochondrial fusion in yeast requires the transmembrane
512 GTPase Fzo1p. *J. Cell Biol.* **143,** 359–73 (1998).
513 10. Mishra, P. & Chan, D. C. Metabolic regulation of mitochondrial dynamics. *J. Cell Biol.*
514 **212,** 379–87 (2016).
515 11. Chen, H. & Chan, D. C. Mitochondrial dynamics--fusion, fission, movement, and
516 mitophagy--in neurodegenerative diseases. *Hum. Mol. Genet.* **18,** R169-76 (2009).
517 12. Hirai, K. *et al.* Mitochondrial abnormalities in Alzheimer's disease. *J. Neurosci.* **21,**
518 3017–23 (2001).
519 13. Deng, H., Dodson, M. W., Huang, H. & Guo, M. The Parkinson's disease genes pink1
520 and parkin promote mitochondrial fission and/or inhibit fusion in Drosophila. *Proc.*
521 *Natl. Acad. Sci.* **105,** 14503–14508 (2008).
522 14. Graves, J. A. *et al.* Mitochondrial Structure, Function and Dynamics Are Temporally
523 Controlled by c-Myc. *PLoS One* **7,** e37699 (2012).
524 15. Ashrafian, H. *et al.* A Mutation in the Mitochondrial Fission Gene Dnm1l Leads to
525 Cardiomyopathy. *PLoS Genet.* **6,** e1001000 (2010).
526 16. Pilling, A. D., Horiuchi, D., Lively, C. M. & Saxton, W. M. Kinesin-1 and Dynein are the
527 primary motors for fast transport of mitochondria in Drosophila motor axons. *Mol. Biol.*
528 *Cell* **17,** 2057–68 (2006).
529 17. Stowers, R. S., Megeath, L. J., Górska-Andrzejak, J., Meinertzhagen, I. A. &
530 Schwarz, T. L. Axonal transport of mitochondria to synapses depends on milton, a
531 novel Drosophila protein. *Neuron* **36,** 1063–77 (2002).
532 18. Glater, E. E., Megeath, L. J., Stowers, R. S. & Schwarz, T. L. Axonal transport of
533 mitochondria requires milton to recruit kinesin heavy chain and is light chain
534 independent. *J. Cell Biol.* **173,** 545–57 (2006).
535 19. van Spronsen, M. *et al.* TRAK/Milton Motor-Adaptor Proteins Steer Mitochondrial
536 Trafficking to Axons and Dendrites. *Neuron* **77,** 485–502 (2013).
537 20. Chen, Y. & Sheng, Z.-H. Kinesin-1-syntaphilin coupling mediates activity-dependent
538 regulation of axonal mitochondrial transport. *J. Cell Biol.* **202,** 351–64 (2013).
539 21. Kang, J.-S. *et al.* Docking of Axonal Mitochondria by Syntaphilin Controls Their
540 Mobility and Affects Short-Term Facilitation. *Cell* **132,** 137–148 (2008).
541 22. Fu, C., Jain, D., Costa, J., Velve-Casquillas, G. & Tran, P. T. Mmb1p binds

542 mitochondria to dynamic microtubules. *Curr. Biol.* **21,** 1431–1439 (2011).
543 23. Li, T., Zheng, F., Cheung, M., Wang, F. & Fu, C. Fission yeast mitochondria are
544 distributed by dynamic microtubules in a motor-independent manner. *Sci. Rep.* **5,**
545 11023 (2015).
546 24. Huh, D. & Paulsson, J. Random partitioning of molecules at cell division. *Proc. Natl.*
547 *Acad. Sci. U. S. A.* **108,** 15004–9 (2011).
548 25. Lawrence, E. & Mandato, C. Mitochondrial inheritance is mediated by microtubules in
549 mammalian cell division. *Commun. Integr. Biol.* **6,** e27557 (2013).
550 26. Yaffe, M. P., Stuurman, N. & Vale, R. D. Mitochondrial positioning in fission yeast is
551 driven by association with dynamic microtubules and mitotic spindle poles. *PNAS*
552 **100,** 11424–11428 (2003).
553 27. Krüger, N. & Tolic, I. M. Association of mitochondria with spindle poles facilitates
554 spindle alignment. *Curr. Biol.* **18,** 646–647 (2008).
555 28. Jajoo, R. *et al.* Accurate concentration control of mitochondria and nucleoids. *Science*
556 *(80-.).* **351,** (2016).
557 29. Bergeland, T., Widerberg, J., Bakke, O. & Nordeng, T. W. Mitotic partitioning of
558 endosomes and lysosomes. *Curr. Biol.* **11,** 644–651 (2001).
559 30. Shima, D. T., Cabrera-Poch, N., Pepperkok, R. & Warren, G. An ordered inheritance
560 strategy for the Golgi apparatus: visualization of mitotic disassembly reveals a role for
561 the mitotic spindle. *J. Cell Biol.* **141,** 955–66 (1998).
562 31. Tischer, C., Brunner, D. & Dogterom, M. Force- and kinesin-8-dependent effects in
563 the spatial regulation of fission yeast microtubule dynamics. *Mol. Syst. Biol.* **5,** 250
564 (2009).
565 32. West, R. R., Malmstrom, T., Troxell, C. L. & McIntosh, J. R. Two related kinesins,
566 klp5+ and klp6+, foster microtubule disassembly and are required for meiosis in
567 fission yeast. *Mol. Biol. Cell* **12,** 3919–32 (2001).
568 33. Browning, H. *et al.* Tea2p is a kinesin-like protein required to generate polarized
569 growth in fission yeast. *J. Cell Biol.* **151,** 15–28 (2000).
570 34. Busch, K. E., Hayles, J., Nurse, P. & Brunner, D. Tea2p Kinesin Is Involved in Spatial
571 Microtubule Organization by Transporting Tip1p on Microtubules. *Dev. Cell* **6,** 831–
572 843 (2004).
573 35. Beinhauer, J. D., Hagan, I. M., Hegemann, J. H. & Fleig, U. Mal3, the fission yeast
574 homologue of the human APC-interacting protein EB-1 is required for microtubule
575 integrity and the maintenance of cell form. *J. Cell Biol.* **139,** 717–28 (1997).
576 36. Pletjushkina, O. Y. *et al.* Effect of oxidative stress on dynamics of mitochondrial
577 reticulum. *Biochim. Biophys. Acta - Bioenerg.* **1757,** 518–524 (2006).
578 37. Ding, R., West, R. R., Morphew, D. M., Oakley, B. R. & McIntosh, J. R. The spindle
579 pole body of Schizosaccharomyces pombe enters and leaves the nuclear envelope
580 as the cell cycle proceeds. *Mol. Biol. Cell* **8,** 1461–79 (1997).
581 38. Birky, C. W. The partitioning of cytoplasmic organelles at cell division. *Int. Rev. Cytol.*
582 *Suppl.* **15,** 49–89 (1983).
583 39. Hennis, A. S. & Birky, C. W. Stochastic partitioning of chloroplasts at cell division in
584 the alga Olisthodiscus, and compensating control of chloroplast replication. *J. Cell*
585 *Sci.* **70,** 1–15 (1984).
586 40. Guillou, E., Bousquet, C., Daloyau, M., Emorine, L. J. & Belenguer, P. Msp1p is an
587 intermembrane space dynamin-related protein that mediates mitochondrial fusion in a
588 Dnm1p-dependent manner in S. pombe. *FEBS Lett.* **579,** 1109–16 (2005).
589 41. Maundrell, K. nmt1 of fission yeast. A highly transcribed gene completely repressed

590 by thiamine. *J. Biol. Chem.* **265,** 10857–64 (1990).
591 42. Brazer, S. W., Williams, H. P. & Chappell, T. G. A fission yeast kinesin affects Golgi
592 membrane recycling. 149–166 (2000).
593 43. Chiron, S., Bobkova, A., Zhou, H. & Yaffe, M. P. CLASP regulates mitochondrial
594 distribution in Schizosaccharomyces pombe. *J. Cell Biol.* **182,** 41–49 (2008).
595 44. Varadi, A. *et al.* Cytoplasmic dynein regulates the subcellular distribution of
596 mitochondria by controlling the recruitment of the fission factor dynamin-related
597 protein-1. *J. Cell Sci.* **117,** 4389–400 (2004).
598 45. Liu, X., Weaver, D., Shirihai, O. & Hajnóczky, G. Mitochondrial 'kiss-and-run':
599 interplay between mitochondrial motility and fusion-fission dynamics. *EMBO J.* **28,**
600 3074–89 (2009).
601 46. Karbowski, M. *et al.* Opposite effects of microtubule-stabilizing and microtubule-
602 destabilizing drugs on biogenesis of mitochondria in mammalian cells. *J. Cell Sci.*
603 **114,** 281–291 (2001).
604 47. Höög, J. L. *et al.* Organization of interphase microtubules in fission yeast analyzed by
605 electron tomography. *Dev. Cell* **12,** 349–61 (2007).
606 48. Mears, J. A. *et al.* Conformational changes in Dnm1 support a contractile mechanism
607 for mitochondrial fission. *Nat. Struct. Mol. Biol.* **18,** 20–26 (2011).
608 49. Taguchi, N., Ishihara, N., Jofuku, A., Oka, T. & Mihara, K. Mitotic phosphorylation of
609 dynamin-related GTPase Drp1 participates in mitochondrial fission. *J. Biol. Chem.*
610 **282,** 11521–9 (2007).
611 50. Chang, C.-R. & Blackstone, C. Cyclic AMP-dependent protein kinase phosphorylation
612 of Drp1 regulates its GTPase activity and mitochondrial morphology. *J. Biol. Chem.*
613 **282,** 21583–7 (2007).
614 51. Han, X.-J. *et al.* CaM kinase Iα–induced phosphorylation of Drp1 regulates
615 mitochondrial morphology. *J. Cell Biol.* **182,** 573–585 (2008).
616 52. Ferreira-da-Silva, A. *et al.* Mitochondrial Dynamics Protein Drp1 Is Overexpressed in
617 Oncocytic Thyroid Tumors and Regulates Cancer Cell Migration. *PLoS One* **10,**
618 e0122308 (2015).
619 53. Itoh, K., Nakamura, K., Iijima, M. & Sesaki, H. Mitochondrial dynamics in
620 neurodegeneration. *Trends Cell Biol.* **23,** 64–71 (2013).
621 54. Dubey, J., Ratnakaran, N. & Koushika, S. P. Neurodegeneration and microtubule
622 dynamics: death by a thousand cuts. *Front. Cell. Neurosci.* **9,** 343 (2015).
623 55. Kroboth, K. *et al.* Lack of Adenomatous Polyposis Coli Protein Correlates with a
624 Decrease in Cell Migration and Overall Changes in Microtubule Stability. *Mol. Biol.*
625 *Cell* **18,** 910–918 (2007).
626 56. Senft, D. & Ronai, Z. A. Regulators of mitochondrial dynamics in cancer. *Curr. Opin.*
627 *Cell Biol.* **39,** 43–52 (2016).
628 57. Forsburg, S. L. & Rhind, N. Basic methods for fission yeast. *Yeast* **23,** 173–183
629 (2006).
630 58. Kanter-Smoler, G., Dahlkvist, A. & Sunnerhagen. Improved Method for rapid
631 Transformation of Intact Schizosaccharomyces pombe cells. *Biotechniques* **16,** 798–
632 800 (1994).
633

634 **Acknowledgements**

635 We thank J. M. Thankachan, S. S. Nuthalapati and M. Ayushman for pilot experiments;
636 High Content Imaging Facility at BSSE, IISc, and P. I. Rajyaguru for the use of the InCell

6000, and Deltavision RT microscopes respectively; P. Delivani, I. Jourdain, R.C. Salas, M. Takaine, I. Tolic, P. Tran, and NBRP Japan for yeast strains and constructs; S. Jain for CellROX reagent. The research was supported by the Department of Science and Technology (India)-INSPIRE Faculty Award, the Department of Biotechnology (India) Innovative Young Biotechnologist Award, and the Science and Engineering Research Board (SERB, India) Early Career Research Award awarded to V.A., and SERB Early Career Research Award awarded to S.J.

Author Contributions

K.M. carried out the Dnm1 experiments, M.K.C. and S. J. carried out and analysed the flow cytometry experiments, V.A. performed all the other experiments and data analysis, designed the project, and wrote the paper.

Competing Financial Interests

The authors declare no competing financial interests.

Extended Data

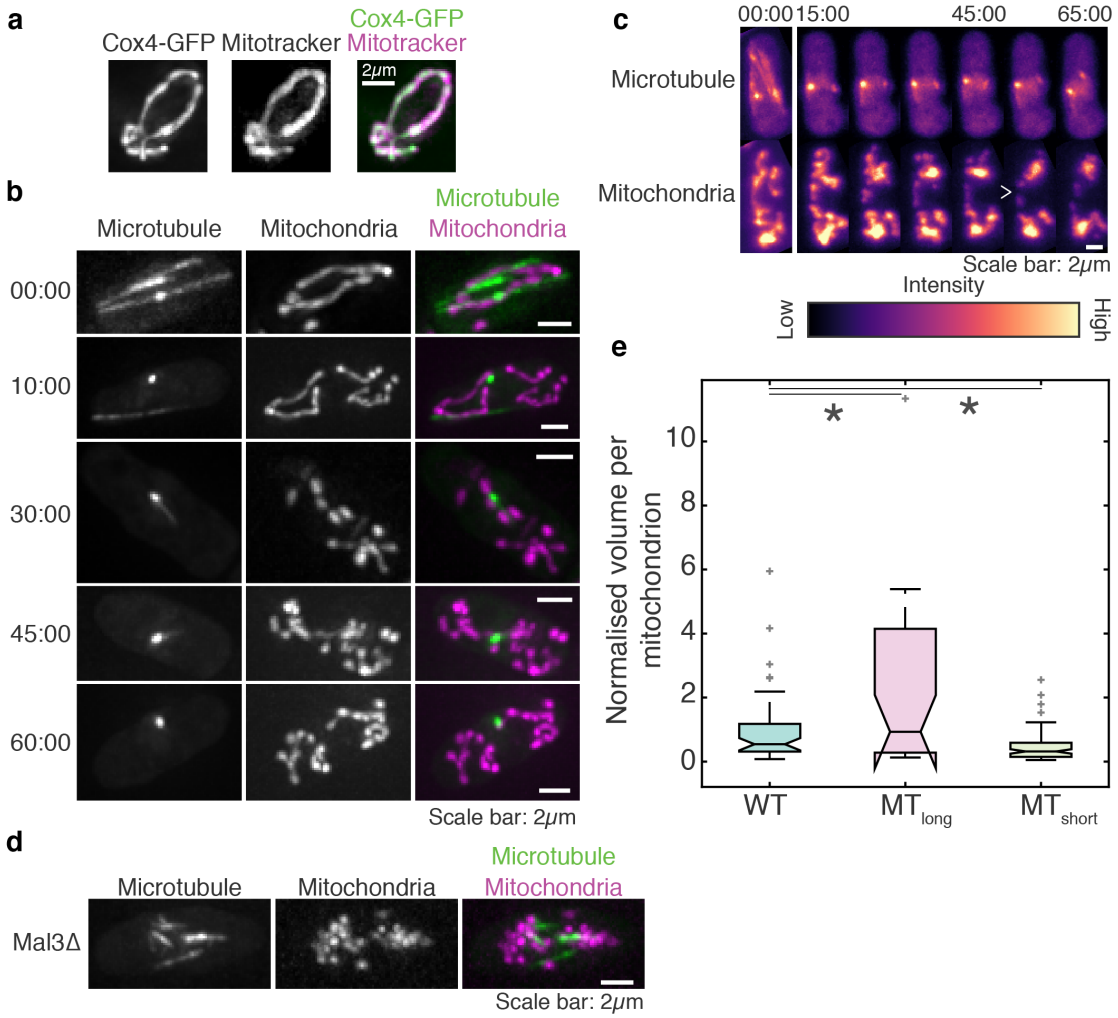

Extended Data Figure 1. Depolymerisation of microtubules increases mitochondrial fission. a, Maximum intensity projections of deconvolved Z-stack images of Cox4-GFP (left), Mitotracker Orange staining (centre) and their composite (right) in interphase cells (strain PT.1650, see Table S1) showing colocalisation of both signal intensities. **b,** Maximum intensity projections of deconvolved Z-stack images of microtubules (left), mitochondria (centre) and their composite (right) in fission yeast cells at the onset of mitosis. Time in mm:ss is indicated to the left of the images. **c,** Montage of maximum intensity projected confocal Z-stack images of microtubule depolymerisation (top) and mitochondria (bottom) of wild-type cells (strain KI001, see Table S1) treated with MBC (see Methods) represented in the intensity map indicated at the bottom of the images. The open white arrowhead indicates a representative fission event. **d,** Box plot of the volume of individual mitochondria in wild-type ('WT'), Klp5Δ/Klp6Δ ('MT_{long}') and Klp4Δ ('MT_{short}') cells normalised to mean mitochondrial volume in wild-type cells (n=49, 28 and 100 mitochondria respectively). Light grey crosses represent outliers, asterisk represents significance ($p<0.05$) and 'n.s.' indicates no significant difference. **e,** Maximum intensity projections of deconvolved Z-stack images of microtubule (left), mitochondria (centre) and their composite (right) in interphase Mal3Δ cells (strain KN001, see Table S1) showing several small mitochondrial fragments similar to those seen in Klp4Δ cells.

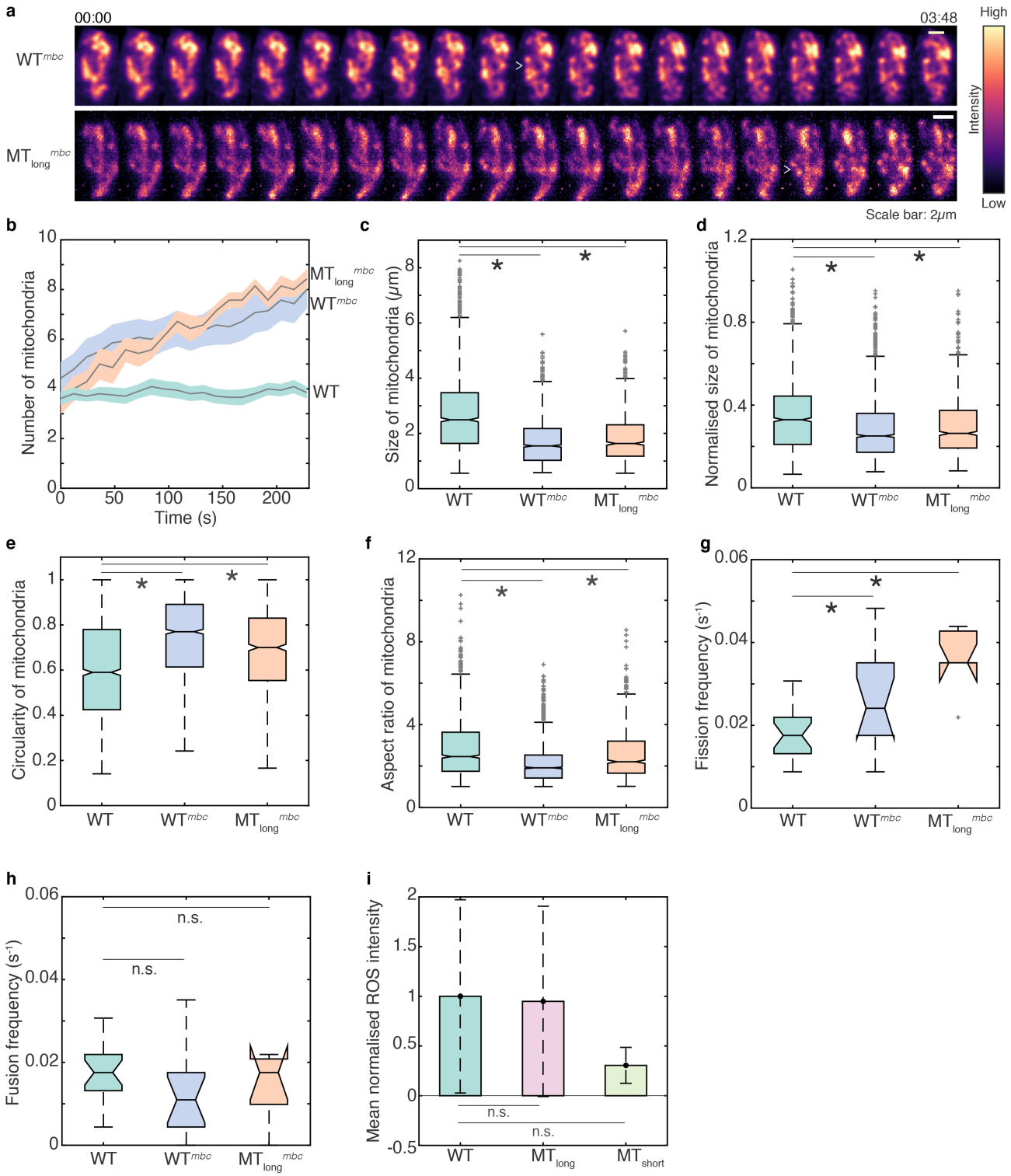

Extended Data Figure 2. Microtubule depolymerisation induces increased fission in Klp5Δ/Klp6Δ cells. a, Montage of maximum intensity projected confocal Z-stack images of MBC-treated wild-type (WT^{mbc}, strain KI001, see Table S1) and Klp5Δ/Klp6Δ ('MT_{long}^{mbc}', strain G3B, see Table S1) cells represented in the intensity map indicated to the right of the images. White open arrowheads point to representative fission events. 00:00 indicates time (mm:ss) 2min after addition of MBC. **b,** Evolution of mitochondrial number with time indicated as mean (solid grey line) and standard error of the mean (shaded region) for wild-type ('WT'), WT^{mbc}, and MT_{long}^{mbc} cells (*n*=21, 14 and 7 cells respectively). **c,** Box plot of the size of mitochondria in WT, WT^{mbc}, and MT_{long}^{mbc} cells,

calculated as the length of the major axis of an ellipse fitted to each mitochondrion (*n*=1613, 1765 and 886 mitochondria respectively). **d,** Box plot of the size of individual mitochondria in WT, WT^{mbc}, and MT_{long}^{mbc} cells normalised to their cell lengths (*n*=1613, 1765 and 886 mitochondria respectively). **e,** Box plot of the circularity of mitochondria in WT, WT^{mbc}, and MT_{long}^{mbc} cells (*n*=1613, 1765 and 886 mitochondria respectively). **f,** Box plot of the aspect ratio of mitochondria in WT, WT^{mbc}, and MT_{long}^{mbc} cells (*n*=1613, 1765 and 886 mitochondria respectively). **g,** Box plot of the fission frequencyof mitochondria per second in WT, WT^{mbc}, and MT_{long}^{mbc} cells (*n*=21, 14 and 7 cells respectively). **h,** Box plot of the fusion frequency of mitochondria per second in WT, WT^{mbc}, and MT_{long}^{mbc} cells (*n*=21, 14 and 7 cells respectively). **i,** Bar plot of cellular ROS measured using flow cytometry (see Supplementary Information) in live WT, MT_{long} and MT_{short} cells normalised to mean of the ROS intensity in WT cells (*n*=3 independent experiments, ≥10,000 events each). Light grey crosses represent outliers, asterisk represents significance ($p<0.05$) and 'n.s.' indicates no significant difference. Note that the WT data represented in this figure is the identical to the wild-type data plotted in Fig. 2 and Extended Data Fig. 2 and has been re-used for comparison.

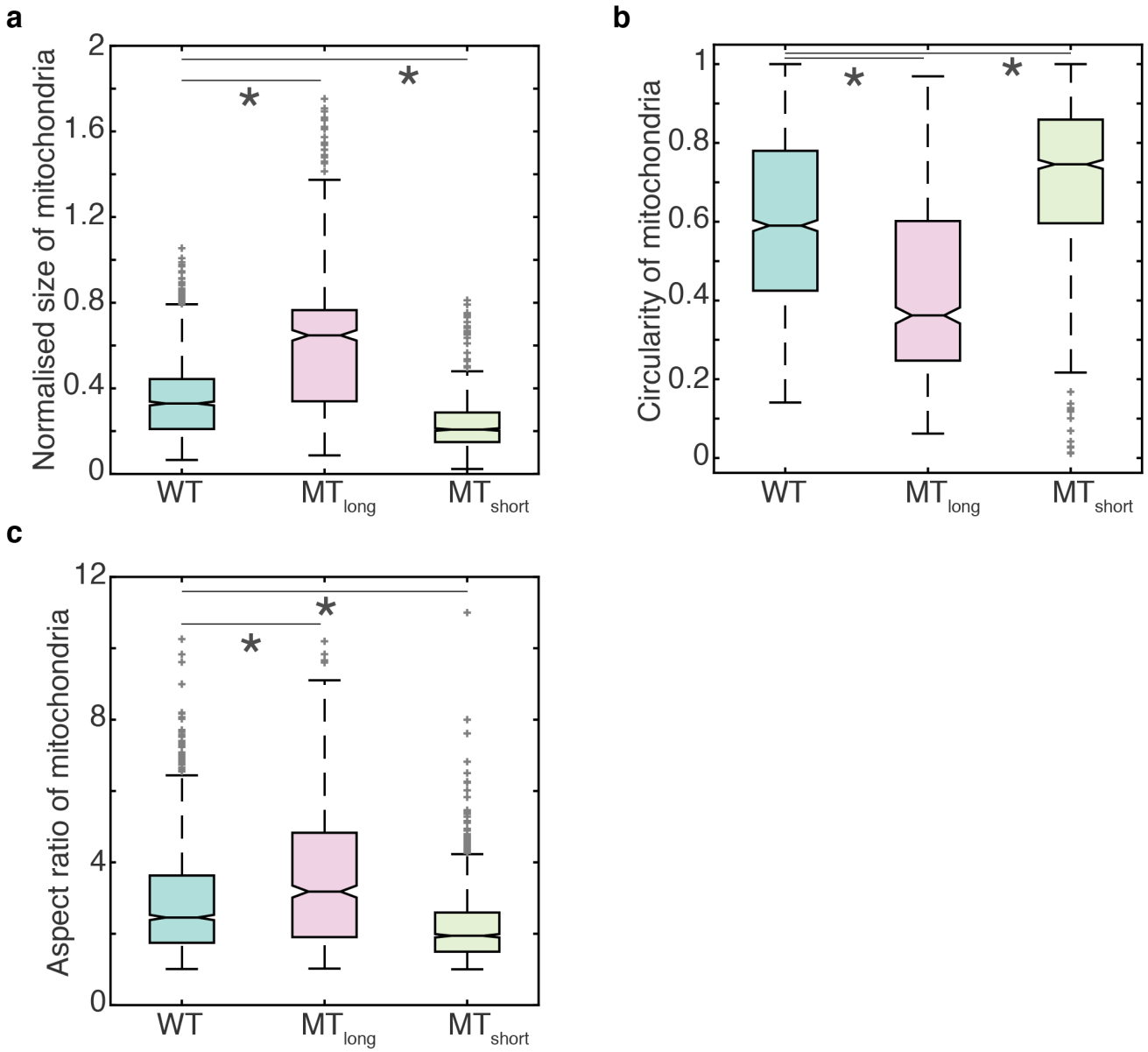

Extended Data Figure 3. Microtubule dynamics determines the morphology of mitochondria. a, Box plot of the size of individual mitochondria in wild-type ('WT'), Klp5Δ/Klp6Δ ('MT_{long}') and Klp4Δ ('MT_{short}') cells normalised to their cell lengths (*n*=1613, 739 and 1326 mitochondria respectively). **b,** Box plot of the circularity of mitochondria in WT, MT_{long} and MT_{short} cells (*n*=1613, 739 and 1326 mitochondria respectively). **c,** Box plot of the aspect ratio of mitochondria in WT, MT_{long} and MT_{short} cells (*n*=1613, 739 and 1326 mitochondria respectively). Error bars represent standard deviation. Light grey crosses represent outliers, asterisk represents significance ($p<0.05$) and 'n.s.' indicates no significant difference.

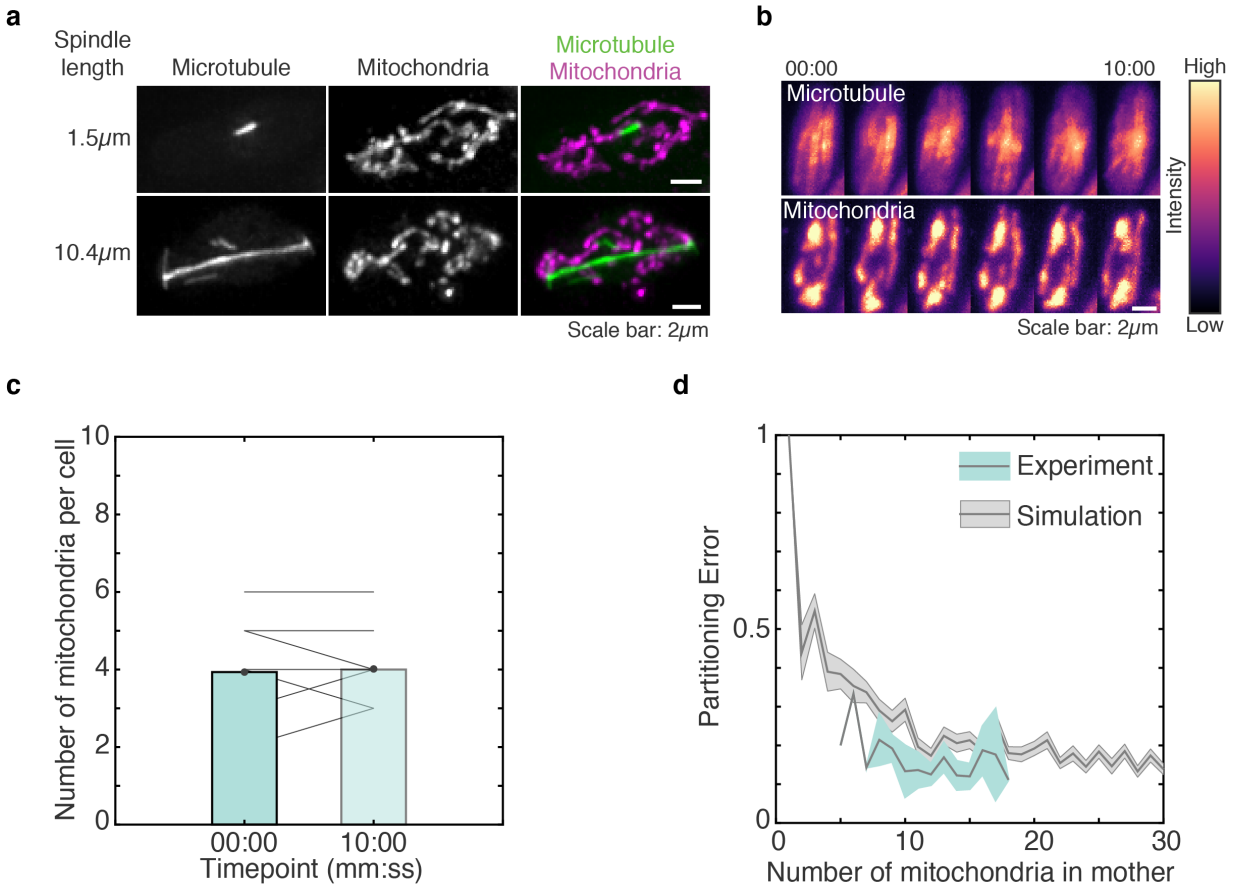

Extended Data Figure 4. Mitotic spindle length does not influence number of mitochondria. a, Maximum intensity projections of deconvolved Z-stack images of the microtubules (left), mitochondria (centre) and their composite (right) of WT cells (strain KI001, see Table S1) with short (top) and long (bottom) mitotic spindles. The length of the spindle is indicated to the left of the images. **b,** Montage of maximum intensity projected confocal Z-stack images of the microtubules (top) and mitochondria (bottom) in a non-mitotic wild-type cell (strain KI001, see Table S1) represented in the intensity map indicated to the right of the images.. **c,** Bar plot of the mean number of mitochondria per cell before ('00:00') and after ('10:00') the same time window for which mitotic cells were monitored in Fig. 3c, d. Solid grey lines represent data from individual cells (*n*=7 cells). **d,** Plot of number of mitochondria in mother cell vs. partitioning error (see Supplementary Information) between daughter cells in simulation (grey) and experiments (blue) expressed as mean (solid grey line) and standard error of the mean (shaded area).

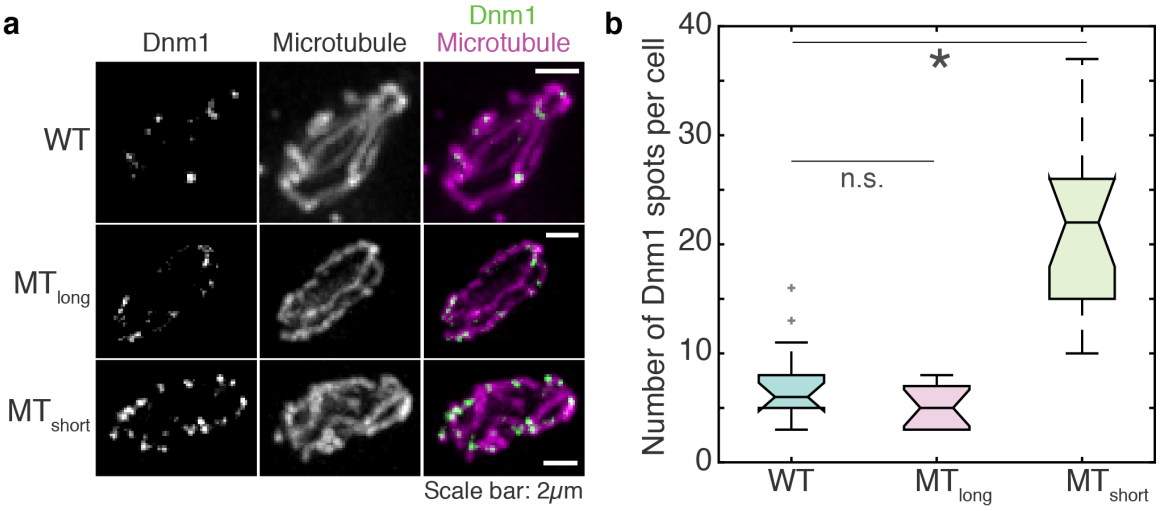

c

Parameter	Value (mean ± s.e.m)		
	WT	MT_{long}	MT_{short}
Number of mitochondria	4.9 ± 0.4	2.3 ± 0.4	10 ± 0.9
Normalised total volume of mitochondria	1.00 ± 0.10	1.09 ± 0.13	0.92 ± 0.07
Normalised volume of individual mitochondria	1.00 ± 0.16	2.30 ± 0.50	0.45 ± 0.04
Size of mitochondria (μm)	2.72 ± 0.03	6.53 ± 0.11	1.77 ± 0.02
Size of mitochondria normalised to cell length	0.35 ± 0.01	0.59 ± 0.01	0.23 ± 0.01
Circularity of mitochondria	0.60 ± 0.01	0.44 ± 0.01	0.71 ± 0.01
Aspect ratio of mitochondria	2.84 ± 0.04	3.55 ± 0.07	2.16 ± 0.03
Mitochondrial fission frequency (s^{-1})	0.018 ± 0.002	0.006 ± 0.001	0.032 ± 0.005
Mitochondrial fusion frequency (s^{-1})	0.017 ± 0.002	0.011 ± 0.001	0.025 ± 0.005

Extended Data Figure 5. Dnm1 spots colocalise with the mitochondria and their number is inversely proportional to the length of microtubules. a, Maximum intensity projections of deconvolved Z-stack images of Dnm1 (left), microtubules (centre) and their composite (right) in wild-type ('WT', strain FY7143 transformed with pREP41-Dnm1-Cterm-GFP, see Table S1), Klp5Δ/Klp6Δ ('MT_{long}', strain FY20823 transformed with pREP41-Dnm1-Cterm-GFP, see Table S1) and Klp4Δ ('MT_{short}', strain Mcl438 transformed with pREP41-Dnm1-Cterm-GFP, see Table S1) cells. **b,** Box plot of the number of Dnm1 spots in WT, MT_{long} and MT_{short} cells (*n*=13, 14, and 18 cells respectively). Note that the mitochondrial morphology in WT, MT_{long} and MT_{short} cells appears abnormal due to inactivity of the GFP-tagged Dnm1. Light grey crosses represent outliers, asterisk represents significance ($p<0.05$) and 'n.s.' indicates no significant difference **c,** Measured parameters relating to mitochondrial numbers and morphology in WT, MT_{long} and MT_{short} interphase cells represented as mean ± s.e.m.

738 **Supplementary Information**

739

740 **Methods**

741 **ROS detection and viability assay using flow cytometry.** A loopful of L972, FY20823 or
742 McI438 cells were inoculated in liquid YE and incubated overnight at 30°C in a shaking
743 incubator. Cells were harvested using a table-top centrifuge (2000g, 30s) and washed three
744 times with 1X PBS. The pellets were re-suspended in 500μl of 1X PBS, containing CellROX
745 (5μM) dye (ThermoFisher, USA). Following incubation at 30°C for 30min, cells were
746 washed three times with 1X PBS. Finally, cell pellets were re-suspended in an appropriate
747 volume of 1X PBS containing propidium iodide (6μg/ml), incubated for 10min at room
748 temperature, and run on a flow cytometer (BD FACS-Celesta). A minimum of 10,000 events
749 of cells was collected, and data analyzed using FlowJo (FlowJo LLC, USA). ROS was
750 reported as median fluorescence intensity for each dataset.

751 **Estimation of partitioning error during cell division.** The partitioning error of
752 mitochondria at cell division between the daughter cells Q_x was calculated from the
753 equation[24]:

$$Q_x^2 = \frac{(L-R)^2}{x^2}$$

754 where L and R were mitochondrial numbers in the resulting daughter cells and x, the
755 number of mitochondria in the mother cell. The data in Extended Data Fig. 4d were
756 simulated by independently assigning x mitochondria with 50% probability to either
757 daughter cell. Simulations were re-run 50 times to obtain the mean and the standard error
758 of the mean depicted in Extended Data Fig. 4d.

759 **Counting of Dnm1 spots.** Dnm1 was visualised in cells grown in the presence of
760 0.05μM thiamine for partial induction of the nmt1 promoter. Even with only partial induction,
761 a majority of the cells showed extremely high expression of Dnm1, with most of the signal
762 concentrated in a single spot in the cell. The rest of the cells showed lower expression, with
763 Dnm1 signal distributed in a few spots across the cell. The latter were chosen for analysis
764 of number of Dnm1 spots. For counting the number of Dnm1 spots in Extended Data Fig.
765 5b, the maximum intensity projection of deconvolved Z-stack images were used. For
766 identification of spots, we set the lower threshold as 60-80% of the maximum intensity in
767 these images. The contrast in the images in Fig. 5a and Extended Fig. 5a reflect these
768 threshold settings.

769 **Table S1**

770

771 **Strains and constructs used in this study**

Name	Phenotype	Source
FY20823	*h- leu1 ura4 his7 Δklp5::ura4+ Δklp6::ura4+*	NBRP, Japan
FY7143	*h- ura4-D18 leu1-32 ade6-M216 his7-366*	Iva Tolić, Croatia
G3B	*h- Δklp5- Δklp6 – nmt1-GFP-atb2 leu ade*	Rafael Carazo Salas, UK
G5B	*h- klp4::kanr nmt1-GFP-atb2 leu ura*	Rafael Carazo Salas, UK
KI001	*h+ sid4-GFP::kanr kanr -nmtP3-GFP-atb2+ nmt1-pCOX4RFP::leu1+ ura4-D18 ade6-M210*	Iva Tolić, Croatia
KN001	*h + Δmal3::his3+ nmt1-pCOX4-dsRed ::leu1+ nmt1-atb1-GFP:LEU2 ade6-M210 ura4-D18 leu1-32 his3D1*	Iva Tolić, Croatia
L972	*h- WT*	Iva Tolić, Croatia
McI438	*h+ tea2d:his3 ade6 leu1-32 ura4-D18 his3-D1*	Iva Tolić, Croatia
MTY271	*h- mCherry-atb2:hphMX6 leu1-32 ura-d18*	Masakatsu Takaine, Japan
PT1650	*h+ cox4-GFP:leu1 ade6-M210 leu1-32 ura4-D18*	Phong Tran, USA
pREP41-Dnm1-Cterm-GFP (plasmid)	*Dnm1-GFP*	Isabelle Jourdain, UK
pREP41-Dnm1 (plasmid)	*Dnm1 (untagged)*	Isabelle Jourdain, UK

772

773 **Table S2**

774

775 **Partitioning of mitochondria between daughter cells.**

n	*x*	*(n-x)*	*N*	*Obs.*	*Exp.*	*Obs.-Exp.*
5	2	3	2	2	1.25	0.75
6	2	4	2	2	0.94	1.06
	3	3		0	0.63	-0.63
7	4	3	3	3	1.64	1.36
8	2	6	7	1	1.53	-0.53
	3	5		4	3.06	0.94
	4	4		2	1.91	0.09
9	3	6	11	4	3.61	0.39
	4	5		7	5.41	1.59
10	3	7	6	1	1.41	-0.41
	4	6		2	2.46	-0.46
	5	5		3	1.48	1.52
11	4	7	4	1	1.29	-0.29
	5	6		3	1.80	1.20
12	5	7	8	6	3.09	2.91
	6	6		2	1.80	0.20
13	5	8	5	3	1.57	1.43
	6	7		2	2.09	-0.09
14	5	9	7	1	1.71	-0.71
	6	8		4	2.57	1.43
	7	7		2	1.47	0.53
15	6	9	5	2	1.53	0.47
	7	8		3	1.96	1.04
16	6	10	2	1	0.49	0.51
	7	9		1	0.70	0.30
	8	8		0	0.40	-0.40
17	6	11	2	1	0.38	0.62
	7	10		0	0.60	-0.60
	8	9		1	0.74	0.26
18	8	10	1	1	0.33	0.67
	9	9		0	0.37	-0.37

776 *n* is the number of mitochondria in the mother, *x* and *n-x* in the daughter cells at cell
777 division. *N* is the number of cells counted with *n* mitochondria in the mother. *Obs.* is the
778 observed number of cells showing partition of *n* into *x* and *n-x*, and *Exp.* is the expected
779 number of cells with the same *x* and *n-x* partition given *N* cells predicted by the binomial
780 distribution.

Supplementary video captions

Video S1. Live-cell confocal microscopy of MBC-treated interphase fission yeast cells with the mitochondria stained with Mitotracker. Warmer colours indicate higher intensities. Images were acquired at 2min intervals. Time 00:00 (mm:ss) indicates time of addition of MBC. Imaging was resumed 15min after MBC addition ('15:00'). Scale bar represents 2μm. This movie corresponds to Extended Data Fig. 1c.

Video S2. 3D projection of microtubules (green) and mitochondria (magenta) in a wild-type cell (strain KI001, see Table S1). This movie corresponds to Fig. 1a.

Video S3. 3D projection of microtubules (green) and mitochondria (magenta, stained with Mitotracker) in a Klp5Δ/Klp6Δ cell (strain G3B, see Table S1). This movie corresponds to Fig. 1a.

Video S4. 3D projection of microtubules (green) and mitochondria (magenta, stained with Mitotracker) in a Klp4Δ cell (strain G5B, see Table S1). This movie corresponds to Fig. 1a.

Video S5. Mitochondrial dynamics in a wild-type cell (strain KI001, see Table S1) stained with Mitotracker. A 5-slice Z-stack with step size of 0.5μm was obtained every 12s. The video represents the maximum-intensity projected images of the stacks obtained. Warmer colours indicate higher intensity. The closed white arrowhead points to a fusion event and the open white arrowhead points to a fission event. Scale bar represents 2μm. This movie corresponds to Fig. 2a.

Video S6. Mitochondrial dynamics in a Klp5Δ/Klp6Δ cell (strain G3B, see Table S1) stained with Mitotracker. A 5-slice Z-stack with step size of 0.5μm was obtained every 12s. The video represents the maximum-intensity projected images of the stacks obtained. Warmer colours indicate higher intensity. The closed white arrowhead points to a fusion event. Scale bar represents 2μm. This movie corresponds to Fig. 2a.

Video S7. Mitochondrial dynamics in a Klp4Δ cell (strain G5B, see Table S1) stained with Mitotracker. A 5-slice Z-stack with step size of 0.5μm was obtained every 12s. The video represents the maximum-intensity projected images of the stacks obtained. Warmer colours indicate higher intensity. The open white arrowhead points to a fission event. Scale bar represents 2μm. This movie corresponds to Fig. 2a.

Video S8. 3D projection of microtubules (green) and mitochondria (magenta) in a wild-type mitotic cell (strain KI001, see Table S1). This movie corresponds to Fig. 3a.

Video S9. Microtubule dynamics (left) and mitochondrial dynamics (right) in a wild-type cell (KI001, see Table S1) at the onset of mitosis. A 5-slice Z-stack with step size of 0.5μm was obtained every 2min. The video represents the maximum-intensity projected images of the stacks obtained. Warmer colours indicate higher intensity. Scale bar represents 2μm. The open white arrowheads point to fission events. This movie corresponds to Fig. 3b.

827 **Video S10.** 3D projection of Dnm1 (green) and microtubules (magenta) in wild-type cells
828 (strain MTY271 transformed with pREP41-Dnm1-Cterm-GFP, see Table S1). This movie
829 corresponds to Fig. 5a.